Astronomy & Astrophysics manuscript no. SPE*2013*Outburst
October 5, 2015

Analysis of the September ϵ-Perseid outburst in 2013

Francisco Espartero[1,2], José M. Madiedo[1,3], Alberto J. Castro-Tirado[4], Jaime Zamorano[5], Josep M. Trigo-Rodriguez[6], José A. Docobo[7], Jaime Izquierdo[5], Juan Lacruz[8], Pedro P. Campo[7], Manuel Andrade[7,9], Sensi Pastor[10], José A. de los Reyes[10], Francisco Ocaña[5], Alejandro Sánchez de Miguel[5], and Pep Pujols[11]

1 Facultad de Ciencias Experimentales, Universidad de Huelva. 21071 Huelva, Spain
2 Observatorio Astronómico de Andalucía, 23688 La Pedriza, Alcalá la Real, Jaén, Spain
3 Departamento de Física Atómica, Molecular y Nuclear. Facultad de Física. Universidad de Sevilla. 41012 Sevilla, Spain
4 Instituto de Astrofísica de Andalucía, CSIC, Apt. 3004, 18080 Granada, Spain
5 Dpto. de Astrofísica y CC. de la Atmósfera, Facultad de Ciencias Físicas, Universidad Complutense de Madrid, 28040 Madrid, Spain
6 Institute of Space Sciences (CSIC-IEEC), Campus UAB, Carrer de Can Magrans, s/n, 08193 Cerdanyola del Vallés (Barcelona), Spain
7 Observatorio Astronómico Ramón María Aller (OARMA). Universidade de Santiago de Compostela, Avenida das Ciencias, Campus Vida. Santiago de Compostela, Spain
8 La Cañada Observatory (MPC J87), Ávila, Spain
9 Departamento de Matemática Aplicada. Escola Politécnica Superior. Universidade de Santiago de Compostela, Campus Universitario, 27002 Lugo, Spain.
10 Observatorio Astronómico de La Murta. Molina de Segura, 30500 Murcia, Spain
11 Agrupació Astronómica d'Osona (AAO), Carrer Pare Xifré 3, 3er. 1a. 08500 Vic, Barcelona, Spain

1 October 2015 / Accepted 1 October 2015

ABSTRACT

We analyze the outburst experienced by the September ϵ-Perseid meteor shower on 9 September 2013. As a result of our monitoring the atmospheric trajectory of 60 multi-station events observed over Spain was obtained and accurate orbital data were derived from them. On the basis of these orbits, we have tried to determine the likely parent body of this meteoroid stream by employing orbital dissimilarity criteria. In addition, the emission spectra produced by 2 events belonging to this meteor shower were also recorded. The analysis of these spectra has provided information about the chemical nature of their progenitor meteoroids. We also present an estimation of the tensile strength for these particles

Key words. meteoroites – meteoroids – meteors

1. Introduction

The September ϵ-Perseid (SPE) meteoroid stream gives rise to an annual display of meteors from about September 7 to September 23, peaking around September 12 (Jenniskens 2006). This minor shower was first observed by Denning (1882), and is currently included in the IAU list of meteor showers with code 208 SPE. No systematic analysis of this shower was performed during the early to mid twentieth century, and the first reliable data about this stream were analyzed in Hoffmeister (1948). The next observations were published by Trigo-Rodríguez (1989), who clearly identified SPE activity over the sporadic background, with often trained and bright meteors exhibiting a peak zenithal hourly rate ZHR = 5 in 1989.

Only two outbursts of SPE meteor activity have been reported. The first of these was unexpected and took place on 9 September 2008, with an activity consisting mostly of bright meteors (Jenniskens et al. 2008; Rendtel and Molau 2010). This outburst was not favourable for observers in Europe. So, despite our systems were monitoring the night sky, we could not record this activity increase. The second SPE outburst occurred on 9 September 2013. It took place between 21h30m and 23h20m UT and was confirmed in Jenniskens (2013). On the basis of the results obtained from the analysis of the 2008 outburst, and by assuming that SPE meteoroids were produced by a long-period comet that ejected these particles before the year 1800 AD, Jenniskens (2013) inferred that this dust trail should encounter Earth on 9 September 2013 at 9d22h15m UT. This is in good agreement with the circumstances of the 2013 SPE outburst. However, the parent comet of this stream has not been identified yet. Accurate orbital data obtained from the analysis of SPE meteors could help to find the likely parent of the September ϵ-Perseids. And meteor spectroscopy can also play an important role to derive information about the chemical nature of these meteoroids and their progenitor body.

Optimal weather conditions over most of the Iberian Peninsula during the first half of September 2013 allowed us to analyze the meteor activity produced by the SPE stream. In this work we focus on the analysis of the 2013 SPE outburst. From our recordings we have obtained orbital information about meteoroids belonging to this poorly known stream. The tensile strength of these particles is also estimated. Besides, 2 emission spectra produced by SPE meteors are also analyzed. These are, to our knowledge, the first SPE spectra discussed in the scientific literature.

2. Instrumentation and data reduction techniques

The meteor observing stations that were involved in the monitoring of the September ϵ-Perseid outburst analyzed here are listed in Table 1. These employ between 3 and 12 high-sensitivity CCD video cameras (models 902H and 902H Ultimate from Watec Co., Japan) to monitor the night sky (Madiedo & Trigo-Rodríguez 2008; Trigo-Rodríguez et al. 2009). Their field of view ranges from 90 x 72 to 14 x 11 degrees. These CCD devices work according to the PAL video standard and, so, they generate interlaced video imagery at 25 fps with a resolution of 720x576 pixels. More details about these devices and the way they are operated are given in (Madiedo 2014). To obtain from the recordings of these cameras the atmospheric trajectory of the meteors and the heliocentric orbit of the meteoroids we have employed the AMALTHEA software (Madiedo et al. 2013a,b), which follows the methods described in Ceplecha (1987).

To record meteor emission we have attached holographic diffraction gratings (with 500 or 1000 lines/mm, depending on the device) to the objective lens of some of the above-mentioned CCD video cameras. With these slitless videospectrographs we can record the emission spectrum of meteors brighter than magnitude -3/-4 (Madiedo et al. 2013c; Madiedo 2014). The analysis of the emission spectra obtained during the SPE observing campaign analyzed here was performed by means of the CHIMET software (Madiedo et al. 2013c).

3. Observations and results

In 2013 our meteor observing stations observed activity from the September ϵ-Perseids from September 1 to September 12. On 9 September 2013, at about 21h35m UT, our CCD video devices registered a marked increase in meteor activity associated with this stream, including some fireballs. A careful checking of these data confirmed the SPE outburst between around 21h35m UT on September 9 and 0h 20m UT on September 10, in good agreement with the circumstances described in Jenniskens (2013). From the analysis of the multi-station events recorded from sites listed in Table 1 we have obtained the atmospheric trajectory of these meteors. However, we just took into consideration those trails for which the convergence angle was above 20 degrees. This is the angle between the two planes delimited by the observing sites and the meteor path in the triangulation and measures the quality of the result (Ceplecha 1987). A total of 60 SPE meteors satisfied this condition. These events are listed in Table 2, which shows the absolute magnitude (M), the initial (preatmospheric) photometric mass of the meteoroid (m_p), the beginning and ending heights (H_b and H_e, respectively), the position (J2000.0) of the geocentric radiant (α_g, δ_g), and the preatmospheric (V_∞) and geocentric (V_g) velocities. A code has been assigned to each event for identification with the format DDYYEE, where DD is the day of the month (which ranges between 01 and 12 for the meteors analyzed here), and YY the last two digits of the recording year. The two digits EE are employed to number meteors recorded during the same night and considered in this analysis, so that 00 is assigned to the first meteor imaged, 01 to the next one and so on. The averaged observed preatmospheric velocity was $V_\infty = 66.3 \pm 0.2$ km s^{-1}. The orbital parameters calculated for the meteoroids that produced these meteors are shown in Table 3.

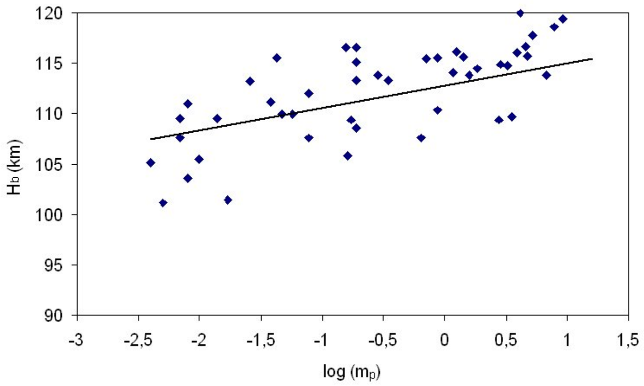

Fig. 1. Meteor beginning height H_b vs. logarithm of the photometric mass m_p of the meteoroid. Solid line: linear fit for measured data.

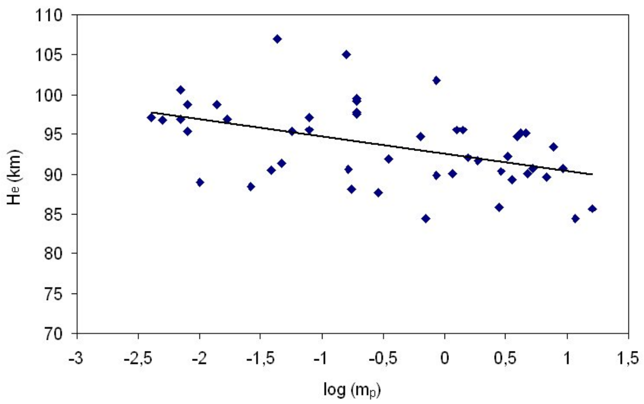

Fig. 2. Meteor ending height H_e vs. logarithm of the photometric mass m_p of the meteoroid. Solid line: linear fit for measured data.

4. Discussion

4.1. Parent body

The averaged orbital data calculated by taking into account a total of N = 60 SPE orbits are shown in Table 3. With these parameters we have obtained that the value of the Tisserand parameter with respect to Jupiter yields $T_J = -0.65 \pm 0.31$. This agrees with the assumption in Jenniskens (2013) that SPE meteoroids are produced by a long period comet.

Besides, we have calculated the so-called K_B parameter, which according to Ceplecha (1988) can be employed to classify meteoroids into four different populations: A-group, comprising particles similar to carbonaceous chondrites ($7.3 \leq K_B < 8$); B-group of dense cometary material ($7.1 \leq K_B < 7.3$); C group of regular cometary material ($6.6 \leq K_B < 7.1$); and D-group of soft cometary material ($K_B < 6.6$). This parameter is defined by the following equation:

$$K_B = log(\rho_B) + 2.5logV_\infty - 0.5log(cos(z_R)) + 0.15 \quad (1)$$

where ρ_B is the air density at the beginning of the luminous trajectory (in g cm^{-3}), V_∞ is the preatmospheric velocity of the meteoroid (in cm s^{-1}), and z_R is the inclination of the atmospheric trajectory with respect to the vertical. We have obtained the air density ρ_B by using the NRLMSISE-00 atmosphere model (Picone et al. 2002). According to our computations, the average K_B parameter for the SPE events in Table 2 yields $K_B = 6.9 \pm$

Table 1. Geographical coordinates of the SPMN meteor observing stations that recorded the 2013 outburst of the SPE meteor shower.

Station #	Station name	Longitude	Latitude (N)	Alt. (m)
1	Sevilla	05º 58' 50" W	37º 20' 46"	28
2	La Hita	03º 11' 00" W	39º 34' 06"	674
3	Huelva	06º 56' 11" W	37º 15' 10"	25
4	Sierra Nevada	03º 23' 05" W	37º 03' 51"	2896
5	El Arenosillo	06º 43' 58" W	37º 06' 16"	40
6	Cerro Negro	06º 19' 35" W	37º 40' 19"	470
7	Avila	04º 29' 30" W	40º 36' 18"	1400
8	Villaverde del Ducado	02º 29' 29"	41º 00' 04"	1100
9	Madrid (UCM)	03º 43' 34" W	40º 27' 03"	640
10	La Murta	01º 12' 10" W	37º 50' 25"	400
11	Folgueroles	02º 19' 33" E	41º 56' 31"	580
12	Montseny	02º 32' 01" E	41º 43' 47"	194
13	Lugo	07º 32' 41" W	42º 59' 35"	418
14	OARMA	08º 33' 34" W	42º 52' 31"	240

0.2. This result suggests that meteoroids in this stream belong to the group of regular cometary materials.

We have tried to determine the likely parent comet of SPE meteoroids by means of orbital dissimilarity criteria (Williams 2011). In this approach we have employed the ORAS program (ORbital Association Software) to search through the Minor Planet Center database in order to establish a potential link between the SPE stream and other bodies in the Solar System (Madiedo et al. 2013d). This analysis has been performed by calculating the Southworth and Hawkings D_{SH} criterion (Southworth & Hawkins 1963). However the lowest values obtained for the DSH function are of about 1.50, which is well above the D_{SH} <0.15 cutoff value usually adopted to validate a potential association (Linblad 1971a,b). So we conclude that the parent comet of the SPE stream is not catalogued.

4.2. Meteor initial and final heights

Figures 1 and 2 show the dependence with meteoroid mass of the beginning and final heights of meteors listed in Table 2, respectively. Figure 1 reveals that the beginning height H_b increases with increasing meteoroid mass, as has been found for other meteor showers with a cometary origin (Koten et al. 2004, Jenniskens 2004, Madiedo 2015). We have described this behaviour by means of a linear relationship between Hb and the logarithm of the photometric mass (solid line in Figure 1). The slope of this line is 2.38 ± 0.70, and this implies that the increase of the beginning height with mass is less pronounced for the September ϵ-Perseids than for the Leonids (a = 9.9 ± 1.5), the Perseids (a = 7.9 ± 1.3), the Taurids (a = 6.6 ± 2.2), and the Orionids (a = 5.02 ± 0.65) (Koten et al. 2004). But more pronounced than for the ρ-Geminids (a = 1.1 ± 0.5), which are produced by tough cometary meteoroids (Madiedo 2015), and the Geminids (a = 0.46 ± 0.26) (Koten et al. 2004), which have an asteroidal origin (Jenniskens 2004). Despite the preatmospheric velocity of the September ϵ-Perseids and the Perseids is similar (~65 km s-1 and ~61 km s^{-1}, respectively), the beginning height exhibited by SPE meteors is significantly lower. Thus, for instance, for SPE meteors H_b is of below 110 km for a meteoroid mass of about 0.02 g (Figure 2), but ~120 km for Perseid members with the same mass (Koten et al. 2004). This suggests that SPE meteoroids are tougher.

The larger is the meteoroid mass, the lower is the terminal point H_e of the meteor (Figure 2). The slope of the line we have employed to model this behaviour (solid line in Figure 2) yields -2.25 ± 0.45. Since slower meteoroids tend to penetrate deeper in the atmosphere, it is not surprising that SPE meteoroids, which exhibit an initial velocity of ~65 km s^{-1}, do not penetrate as deep as the Perseids with a preatmospheric velocity of ~61 km s^{-1} (Koten 2004), the Geminids with a velocity of ~36 km s^{-1} (Jenniskens 2004), or the ρ-Geminids with a velocity of about 23 km s^{-1} (Madiedo 2015).

4.3. Meteoroid strength

The tensile strength of meteoroids ablating in the atmosphere can be estimated by analyzing the flares exhibited by the corresponding meteors. According to this approach, these flares take place as a consequence of the sudden break-up of the meteoroid when the aerodynamic pressure overcomes the strength of the particle (Trigo-Rodríguez & Llorca 2006). However, SPE events listed in Table 2 exhibited a quasi-continuous ablation behaviour, with smooth lightcurves that revealed that no flares occurred during their interaction with the atmosphere. So, we have employed this technique to evaluate the maximum aerodynamic pressure suffered by SPE meteoroids, which has provided a lower limit for their tensile strength. This aerodynamic pressure S can be estimated by using the following relationship (Bronshten 1981):

$$S = \rho_{atm} v^2, \quad (2)$$

where ρ_{atm} and v are the atmospheric density and meteor velocity at a given height, respectively. In this work we have calculated the air density by employing the NRLMSISE-00 atmosphere model (Picone et al. 2002). From the analysis of the atmospheric trajectory calculated for meteors in Table 2 we have obtained a maximum aerodynamic pressure of (2.9 ± 0.3)x10^5 dyn cm^{-2}. This value is higher than the average strength found for Quadrantid and Perseid meteoroids (~2x10^5 dyn cm-2 and (1.2 ± 0.3)x10^5 dyn cm^{-2}, respectively), and below the strength of the Taurids ((3.4 ± 0.7)x10^5 dyn cm^{-2}) (Trigo-Rodríguez & Llorca 2006, 2007).

4.4. Emision spectra

The video spectrographs operated at stations 1 to 6 in Table 1 recorded a total of 8 SPE emission spectra during the outburst recorded on September 9-10. Unfortunately 6 of these were too dim to be analyzed, but the other two had enough quality to provide an insight into the chemical nature of these meteoroids. These spectra were produced by meteors labelled as 091327 and 091331 in Table 2, respectively. They have been analyzed by

Table 2. Trajectory and radiant data (J2000) for the double-station September ϵ-Perseid meteors discussed in the text.

Meteor code	Date	Time (UT) ±0.1s	M ±0.5	m_p (g)	H_p (km) ±0.5	H_e (km) ±0.5	α_g (°)	δ_g (°)	V_∞ km s^{-1}	V_g km s^{-1}
011301	Sep 1	4h16m25.8s	-2.0	0.174±0.070	109.4	88.0	56.99±0.08	42.33±0.08	68.3±0.2	67.3±0.2
011302	Sep 1	20h50m52.3s	1.2	0.007±0.002	109.5	100.6	48.78±0.09	34.88±0.07	68.8±0.2	67.6±0.2
011303	Sep 1	23h22m20.4s	-2.1	0.192±0.078	116.6	99.5	47.20±0.07	34.60±0.05	68.4±0.2	67.1±0.2
021301	Sep 2	1h15m45.0s	-0.5	0.038±0.015	111.2	90.5	47.80±0.09	34.99±0.08	68.4±0.2	67.3±0.2
021302	Sep 2	2h44m43.2s	-1.2	0.078±0.031	112.1	95.6	46.41±0.05	39.02±0.05	67.3±0.2	66.2±0.2
031301	Sep 3	1h25m30.3s	-2.7	0.350±0.142	113.3	92.0	44.20±0.09	39.74±0.06	66.4±0.1	65.2±0.1
031302	Sep 3	3h53m12.9s	-0.7	0.047±0.019	109.9	91.4	46.25±0.08	36.87±0.08	67.4±0.1	66.4±0.1
041301	Sep 4	1h04m43.8s	0.5	0.014±0.005	109.5	98.8	48.09±0.09	36.81±0.07	67.8±0.2	66.6±0.2
051301	Sep 5	1h17m19.2s	-2.5	0.287±0.116	113.9	87.6	45.10±0.06	38.63±0.04	66.5±0.1	65.3±0.1
051302	Sep 5	21h11m18.1s	-3.6	0.863±0.350	115.6	101.8	44.95±0.04	38.62±0.08	66.2±0.1	65.0±0.1
061301	Sep 6	4h59m48.6s	-3.9	1.165±0.473	114.1	90.1	54.52±0.10	39.86±0.09	67.9±0.2	67.0±0.2
081301	Sep 8	2h21m15.4s	1.1	0.008±0.003	107.6	96.9	51.14±0.07	36.72±0.08	67.6±0.2	66.5±0.2
081302	Sep 8	3h29m08.9s	-3.6	0.863±0.350	110.4	89.8	46.83±0.06	40.42±0.06	65.6±0.1	64.6±0.1
081303	Sep 8	4h00m40.7s	-3.4	0.706±0.286	115.4	84.4	45.97±0.05	38.26±0.05	65.8±0.2	64.8±0.2
091301	Sep 9	0h13m42.3s	0.8	0.010±0.004	105.5	89.0	41.54±0.10	39.72±0.05	64.1±0.2	62.9±0.2
091302	Sep 9	0h52m35.4s	1.0	0.008±0.003	111.0	95.4	47.16±0.09	41.02±0.07	65.6±0.2	64.4±0.2
091303	Sep 9	1h31m29.7s	-2.1	0.198±0.078	113.3	97.6	49.36±0.08	38.94±0.09	66.6±0.1	64.5±0.1
091304	Sep 9	1h37m55.5s	1.5	0.005±0.002	101.1	96.8	47.06±0.07	37.52±0.08	66.2±0.1	65.1±0.1
091305	Sep 9	2h34m02.9s	-0.9	0.057±0.023	109.9	95.4	48.38±0.06	38.02±0.05	66.4±0.1	65.3±0.1
091306	Sep 9	21h43m34.0s	-1.2	0.078±0.031	107.6	97.2	45.14±0.08	38.93±0.07	65.2±0.2	63.9±0.2
091307	Sep 9	21h53m24.2s	-5.1	3.87±1.57	116.1	94.8	47.75±0.07	39.02±0.04	65.9±0.2	64.7±0.2
091308	Sep 9	21h56m32.7s	-1.9	0.157±0.063	116.6	105.0	47.82±0.10	38.95±0.06	66.0±0.2	64.8±0.2
091309	Sep 9	21h56m51.3s	-3.4	0.721±0.290	114.3	85.1	48.93±0.07	39.85±0.07	66.1±0.2	64.8±0.2
091310	Sep 9	21h58m13.5s	0.1	0.009±0.003	101.7	97.1	49.54±0.09	38.29±0.09	66.6±0.1	65.3±0.1
091311	Sep 9	22h00m44.5s	0.3	0.017±0.007	101.5	96.9	49.02±0.09	39.96±0.07	66.2±0.1	64.9±0.1
091312	Sep 9	22h00m56.1s	-2.8	0.390±0.149	115.2	88.1	45.90±0.07	39.77±0.03	65.2±0.2	64.0±0.2
091313	Sep 9	22h01m17.6s	-5.7	7.5±3.0	118.2	87.3	47.45±0.06	41.63±0.06	65.3±0.2	64.1±0.2
091314	Sep 9	22h02m23.9s	-0.5	0.035±0.015	105.1	95.9	52.33±0.05	39.75±0.04	67.1±0.1	65.8±0.1
091315	Sep 9	22h04m01.2s	-2.2	0.205±0.083	112.9	97.2	53.34±0.06	38.84±0.07	67.5±0.1	66.2±0.1
091316	Sep 9	22h04m20.3s	-5.2	4.58±1.86	116.7	95.2	47.25±0.05	39.10±0.05	65.7±0.1	64.5±0.1
091317	Sep 9	22h04m46.8s	1.5	0.004±0.001	100.5	96.3	48.81±0.10	40.57±0.05	65.6±0.2	64.9±0.2
091318	Sep 9	22h05m04.0s	-0.6	0.043±0.017	115.6	107.1	48.90±0.06	38.45±0.04	66.3±0.2	65.0±0.2
091319	Sep 9	22h08m10.7s	-3.0	0.480±0.198	111.9	95.1	50.19±0.11	37.75±0.06	66.9±0.1	65.6±0.1
091320	Sep 9	22h09m57.0s	-1.8	0.140±0.050	113.0	97.0	50.52±0.09	41.48±0.07	66.2±0.1	64.9±0.1
091321	Sep 9	22h13m24.3s	-4.6	2.5±1.0	115.2	86.1	50.89±0.08	39.17±0.05	66.8±0.2	65.5±0.2
091322	Sep 9	22h14m05.1s	-0.1	0.026±0.010	113.2	88.4	46.15±0.07	38.48±0.08	65.6±0.1	64.3±0.1
091323	Sep 9	22h16m00.4s	0.0	0.008±0.002	101.3	96.1	47.84±0.05	39.52±0.03	65.9±0.1	64.6±0.1
091324	Sep 9	22h16m48.9s	0.5	0.004±0.001	101.7	97.4	45.65±0.10	39.90±0.07	65.1±0.1	63.8±0.1
091325	Sep 9	22h17m19.4s	-2.1	0.196±0.079	115.1	99.1	48.42±0.08	38.90±0.08	66.2±0.2	64.9±0.2
091326	Sep 9	22h28m32.1s	-5.1	4.14±1.68	120.0	95.1	48.47±0.06	40.54±0.06	65.9±0.2	64.6±0.2
091327	Sep 9	22h34m10.6s	-5.8	7.76±3.14	118.6	93.4	48.55±0.05	38.64±0.04	66.3±0.1	65.0±0.1
091328	Sep 9	22h49m01.2s	-4.9	3.28±1.33	114.8	92.2	46.90±0.10	39.45±0.05	65.6±0.1	64.3±0.1
091329	Sep 9	22h52m36.7s	-4.8	2.87±1.16	114.9	90.4	48.15±0.07	39.34±0.04	65.9±0.2	64.6±0.2
091330	Sep 9	23h01m55.9s	1.0	0.008±0.003	103.6	98.7	46.10±0.10	38.55±0.07	65.5±0.2	64.2±0.2
091331	Sep 9	23h17m15.1s	-5.3	5.23±2.12	117.8	90.7	47.36±0.09	38.67±0.07	65.8±0.1	64.5±0.1
091332	Sep 9	23h23m59.8s	-4.0	1.425±0.578	109.7	95.6	46.03±0.05	38.58±0.06	65.4±0.2	64.1±0.2
091333	Sep 9	23h53m01.0s	-3.3	0.639±0.259	112.6	94.7	48.85±0.08	38.10±0.05	66.4±0.2	65.2±0.2
101301	Sep 10	1h46m40.3s	-4.7	2.77±1.12	109.4	85.8	49.25±0.01	40.17±0.02	65.9±0.1	64.8±0.1
101302	Sep 10	2h45m22.9s	1.8	0.004±0.001	105.2	97.2	47.14±0.03	38.72±0.02	65.5±0.1	64.4±0.1
101303	Sep 10	3h16m23.7s	-6.1	11.6±4.7	120.7	84.4	52.64±0.05	38.78±0.02	67.1±0.1	66.0±0.1
101304	Sep 10	4h07m48.6s	-4.1	1.575±0.639	113.9	92.1	52.76±0.05	38.79±0.02	66.0±0.1	66.0±0.1
101305	Sep 10	4h32m30.8s	-6.4	16.1±6.5	115.9	85.6	52.07±0.05	38.59±0.02	66.8±0.2	65.8±0.2
101306	Sep 10	5h16m42.5s	-5.6	6.73±2.77	113.8	89.6	45.14±0.09	36.52±0.04	65.1±0.2	64.2±0.2
111301	Sep 11	3h43m32.7s	-3.9	1.246±0.505	116.2	95.6	49.33±0.06	40.15±0.03	65.6±0.2	64.6±0.2
111302	Sep 11	4h52m52.0s	-5.2	4.73±1.92	115.8	90.1	48.04±0.05	39.67±0.03	65.2±0.2	64.3±0.2
111303	Sep 11	5h06m46.6s	-4.3	0.860±0.755	114.5	91.7	51.88±0.07	40.65±0.04	66.1±0.2	65.2±0.2
121301	Sep 12	0h26m38.1s	-2.0	0.200±0.079	108.5	97.8	53.38±0.08	37.91±0.05	67.1±0.2	65.9±0.2
121302	Sep 12	0h37m57.9s	-4.9	3.50±1.42	105.7	89.3	49.97±0.05	40.23±0.05	65.7±0.2	64.5±0.2
121303	Sep 12	2h11m22.1s	-1.8	0.163±0.066	105.8	90.6	50.43±0.06	39.73±0.05	65.9±0.1	64.8±0.1
121304	Sep 12	23h24m55.5s	-5.9	9.11±3.69	119.5	90.7	51.15±0.08	41.99±0.05	65.5±0.1	64.3±0.1

Table 3. Orbital data (J2000) for the September ϵ-Perseid meteors listed in Table 2, and averaged orbit for N = 60 SPE meteors.

Meteor code	a (AU)	e	i (°)	Ω $\pm10^{-5}$(°)	ω (°)	q (AU)	T_J
011301	27.3±13.6	0.963±0.018	142.66±0.08	158.71769	194.7±0.2	0.892±0.007	-0.78±0.41
011302	31.5±18.4	0.972±0.015	150.62±0.07	159.38626	225.0±0.2	0.862±0.002	-0.83±0.48
011303	24.7±11.2	0.966±0.015	150.01±0.08	159.48804	229.9±0.5	0.831±0.002	-0.76±0.38
021301	27.8±14.2	0.969±0.015	149.76±0.08	159.56426	228.0±0.5	0.844±0.002	-0.78±0.42
021302	33.2±20.1	0.974±0.015	142.38±0.09	159.62380	225.8±0.4	0.857±0.002	-0.74±0.45
031301	27.5±7.0	0.970±0.007	139.32±0.11	160.53864	232.5±0.3	0.814±0.001	-0.65±0.18
031302	33.5±10.5	0.975±0.007	145.34±0.11	160.63813	232.3±0.3	0.814±0.001	-0.76±0.23
041301	28.4±14.8	0.970±0.015	146.38±0.13	161.49348	230.9±0.5	0.824±0.002	-0.74±0.41
051301	34.8±11.3	0.977±0.007	140.92±0.11	162.47090	237.8±0.3	0.775±0.001	-0.69±0.23
051302	28.6±14.8	0.973±0.013	140.39±0.12	163.27478	240.7±0.5	0.754±0.002	-0.64±0.37
061301	29.4±15.9	0.969±0.016	144.69±0.16	163.59041	218.1±0.4	0.890±0.002	-0.77±0.43
081301	33.5±20.6	0.976±0.014	147.22±0.15	165.42431	235.8±0.4	0.789±0.002	-0.76±0.47
081302	29.3±7.9	0.974±0.006	138.01±0.13	165.46988	240.1±0.3	0.757±0.002	-0.62±0.18
081303	34.3±21.1	0.979±0.012	140.73±0.12	165.49119	245.4±0.6	0.716±0.002	-0.65±0.42
091301	32.4±18.6	0.980±0.011	133.77±0.14	166.30907	254.2±0.6	0.644±0.003	-0.52±0.34
091302	33.6±20.2	0.977±0.013	136.91±0.12	166.33534	240.8±0.5	0.751±0.002	-0.62±0.40
091303	35.1±11.3	0.978±0.006	141.92±0.09	166.36167	239.5±0.3	0.761±0.001	-0.70±0.22
091304	39.2±14.0	0.982±0.006	142.38±0.09	166.36602	246.7±0.3	0.705±0.001	-0.69±0.24
091305	34.3±10.9	0.978±0.006	142.63±0.12	166.40387	243.2±0.3	0.733±0.001	-0.68±0.22
091306	33.0±20.7	0.980±0.012	137.93±0.15	167.17933	250.9±0.6	0.671±0.003	-0.59±0.39
091307	30.8±17.2	0.976±0.012	140.07±0.12	167.18600	245.4±0.6	0.716±0.002	-0.63±0.38
091308	37.8±26.1	0.981±0.013	140.28±0.14	167.18812	245.2±0.6	0.717±0.003	-0.66±0.46
091309	27.9±14.1	0.973±0.013	139.69±0.13	167.18832	241.6±0.6	0.745±0.002	-0.62±0.36
091310	36.8±12.8	0.980±0.006	142.63±0.15	167.18929	243.0±0.3	0.734±0.002	-0.69±0.24
091311	36.7±12.6	0.979±0.007	139.63±0.12	167.19094	241.0±0.3	0.749±0.002	-0.67±0.23
091312	26.6±12.7	0.973±0.012	137.25±0.12	167.19104	248.2±0.6	0.694±0.002	-0.56±0.32
091313	30.4±16.6	0.975±0.013	135.61±0.14	167.19125	242.3±0.6	0.740±0.002	-0.59±0.36
091314	34.2±10.7	0.976±0.007	142.38±0.07	167.19210	234.2±0.2	0.799±0.001	-0.72±0.22
091315	31.3±9.1	0.974±0.007	144.51±0.06	167.19325	233.2±0.3	0.807±0.001	-0.73±0.22
091316	28.0±7.1	0.974±0.006	139.50±0.09	167.19337	246.4±0.3	0.708±0.001	-0.60±0.17
091317	26.4±12.6	0.971±0.013	138.44±0.14	167.19364	240.8±0.3	0.752±0.002	-0.60±0.34
091318	25.0±11.3	0.970±0.013	141.89±0.11	167.19390	244.1±0.6	0.727±0.002	-0.61±0.33
091319	33.6±10.7	0.977±0.007	144.09±0.12	167.19604	241.9±0.3	0.743±0.002	-0.70±0.23
091320	28.5±7.6	0.972±0.007	138.30±0.12	167.19714	235.8±0.3	0.789±0.001	-0.63±0.19
091321	30.5±17.0	0.974±0.014	142.28±0.14	167.19953	238.6±0.6	0.770±0.002	-0.68±0.40
091322	35.0±11.4	0.980±0.006	139.56±0.08	167.19995	249.6±0.3	0.682±0.002	-0.63±0.21
091323	32.2±18.7	0.977±0.012	139.36±0.11	167.20124	244.4±0.3	0.724±0.002	-0.63±0.39
091324	26.9±6.8	0.974±0.006	136.82±0.13	167.20174	248.5±0.3	0.691±0.002	-0.55±0.17
091325	34.2±21.3	0.978±0.013	140.83±0.16	167.20215	244.1±0.5	0.726±0.003	-0.66±0.43
091326	33.9±20.8	0.978±0.013	138.26±0.16	167.20968	241.4±0.6	0.747±0.003	-0.64±0.41
091327	36.6±12.3	0.980±0.006	141.36±0.11	167.21353	244.2±0.3	0.725±0.001	-0.68±0.23
091328	30.3±8.4	0.976±0.006	138.65±0.11	167.22351	246.6±0.3	0.706±0.001	-0.60±0.18
091329	24.4±10.7	0.970±0.012	139.83±0.12	167.22594	244.5±0.3	0.724±0.002	-0.58±0.32
091330	30.4±16.8	0.977±0.012	139.35±0.16	167.23222	249.8±0.6	0.680±0.003	-0.60±0.37
091331	26.1±6.4	0.973±0.006	140.24±0.13	167.24258	247.2±0.3	0.702±0.002	-0.59±0.17
091332	26.2±12.4	0.974±0.012	139.21±0.16	167.24711	250.2±0.6	0.678±0.003	-0.57±0.32
091333	32.3±18.9	0.977±0.013	142.43±0.14	167.26676	244.7±0.6	0.721±0.003	-0.66±0.41
101301	27.0±6.5	0.972±0.006	139.25±0.05	167.53421	241.5±0.3	0.746±0.001	-0.61±0.17
101302	25.1±5.6	0.972±0.006	139.88±0.06	167.38302	248.0±0.3	0.696±0.001	-0.57±0.16
101303	33.0±9.9	0.976±0.007	144.07±0.05	167.40403	235.5±0.2	0.791±0.001	-0.73±0.22
101304	32.2±9.4	0.975±0.007	144.04±0.06	167.62946	235.9±0.2	0.788±0.001	-0.72±0.21
101305	36.8±12.9	0.971±0.013	143.94±0.09	167.45540	237.4±0.5	0.777±0.002	-0.68±0.37
101306	36.1±23.4	0.982±0.011	141.76±0.13	167.48519	256.0±0.6	0.627±0.003	-0.62±0.42
111301	29.1±15.1	0.974±0.012	138.91±0.11	168.39367	243.8±0.5	0.728±0.002	-0.61±0.36
111302	29.3±15.3	0.976±0.012	138.57±0.11	168.44115	247.4±0.6	0.700±0.003	-0.60±0.35
111303	33.4±20.1	0.976±0.013	140.06±0.11	168.45056	237.6±0.4	0.775±0.002	-0.67±0.42
121301	32.1±18.8	0.976±0.013	145.25±0.12	169.23401	240.6±0.6	0.753±0.002	-0.71±0.43
121302	29.0±15.1	0.975±0.012	138.83±0.12	169.24155	244.8±0.6	0.721±0.002	-0.61±0.36
121303	34.7±10.9	0.979±0.006	140.01±0.09	169.30468	244.6±0.3	0.721±0.001	-0.65±0.21
121304	34.8±11.1	0.978±0.006	136.52±0.10	170.16519	242.0±0.3	0.741±0.001	-0.62±0.21
Average	31.2±13.9	0.975±0.011	141.14±0.11	167.81204	241.0±0.4	0.749±0.002	-0.65±0.31

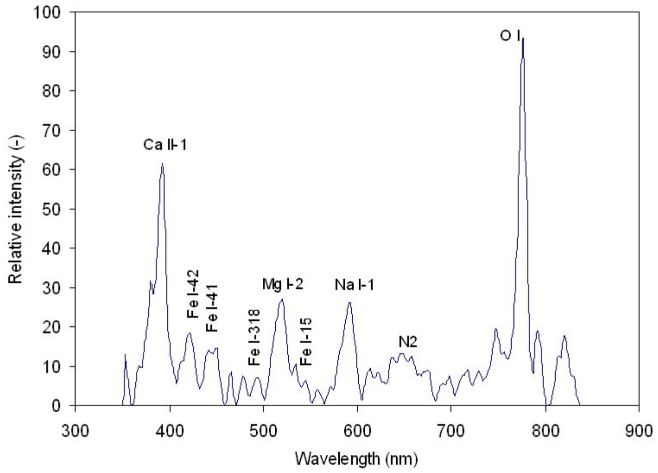

Fig. 3. Calibrated emission spectrum of the 091327 meteor.

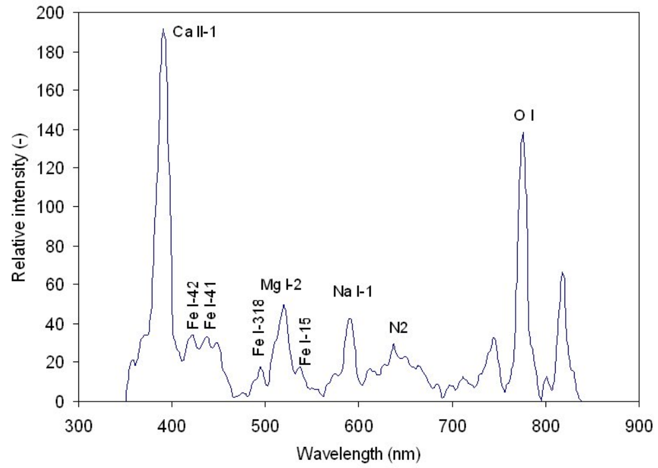

Fig. 4. Calibrated emission spectrum of the 091331 meteor.

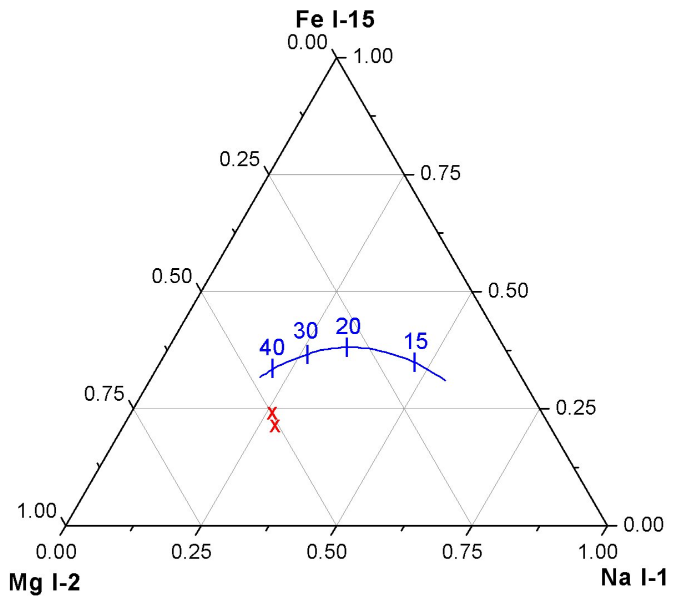

Fig. 5. Expected relative intensity (solid line), as a function of meteor velocity (in km s^{-1}), of the Na I-1, Mg I-2 and Fe I-15 multiplets for chondritic meteoroids (Borovička et al., 2005). Crosses: experimental relative intensities obtained for the 091327 and 091331 spectra.

means of the CHIMET software (Madiedo et al. 2013c). After deinterlacing the video files containing these signals, each video frame was dark-frame subtracted and flat-fielded. Next, a calibration in wavelength was performed by identifying typical lines exhibited by meteor spectra. Then, the intensity of the signals was corrected by taking into account the spectral efficiency of the spectrograph. The results are shown in Figures 3 and 4, where multiplet numbers are given according to Moore (1945). The most noticeable emissions correspond to the atmospheric O I line at 777.4 nm, and to the K and H lines of ionized calcium at 393.3 and 396.8 nm respectively. These two Ca II lines appear blended in the spectrum. Other prominent contributions are those of Fe I-41 (440.4 nm), the Mg I-2 triplet (517.3 nm), and the Na I-1 doublet (588.9 nm). The emission of atmospheric N2 bands was also identified in the red region of the spectrum.

As in previous works (see e.g. Madiedo et al. 2014), we have investigated the chemical nature of the progenitor meteoroids by analyzing the relative intensity of the Na I-1, Mg I-2 and Fe I-15 multiplets in these spectra (Borovička et al. 2005). To perform this analysis the intensity of these emission lines was measured frame by frame and then corrected for the instrumental efficiency. Next the contributions in each frame were added to obtain the integrated intensity for each line along the meteor path. In this way we have obtained for the 091327 and 091331 spectra a Na to Mg intensity ratio of 0.62 and 0.58, respectively. And the Fe/Mg intensity ratio yields 0.33 and 0.41, respectively. The ternary diagram in Figure 5 shows the relative intensity of the emission from the Na I-1, Mg I-2 and Fe I-15 multiplets for both spectra. The solid curve in this plot corresponds to the expected relative intensity, as a function of meteor velocity, for chondritic meteoroids (Borovička et al. (2005)). The position on this solid line corresponding to the velocity of SPE meteors (~65 km s^{-1}) is not explicitly specified in the work published by Borovička et al. (2005) (see Figure 6 in that work), although the authors of that paper indicate that the points describing these high-speed meteors are located near the left edge of this curve. By taking this into account we conclude that the points in this diagram describing both spectra show that SPE meteoroids can be regarded as normal according to the classification given by Borovička et al. (2005). Thus, the position of these experimental points fit fairly well the expected relative intensity for chondritic meteoroids for a meteor velocity of ~65 km s^{-1}.

5. Conclusions

We have analyzed the meteor activity associated with the September ϵ-Perseid meteoroid stream in 2013. In this context we have observed the outburst experienced by this meteor shower on September 9-10. From the analysis of our recordings we have reached the following conclusions:

1) The dependence with meteoroid mass of the initial height observed for SPE meteors reveals a cometary origin for this stream. The analysis of the K_B parameter suggests that these meteoroids consist of regular cometary material.

2) The orbital data calculated from the analysis of our double-station meteors support the idea that SPE meteoroids are associated with a long period comet. However, no parent body could be identified among the objects currently included in the Minor Planet Center database. From this we conclude that the progenitor comet of this meteoroid stream is not yet catalogued.

3) The tensile strength of these meteoroids has been constrained. According to our calculations, the maximum aerodynamic pressure suffered by SPE meteoroids is higher than the tensile strength found for Quadrantid and Perseid meteoroids.

4) We have recorded 8 emission spectra produced by SPE meteors during the outburst recorded on September 9-10. Only two of them had enough quality to be analyzed, and these suggest a chondritic nature for SPE meteoroids.

References

Borovička J., Koten P. Spurny P., Boček J. & Stork R., 2005, Icarus, 174, 15.
Bronshten V.A., 1981, Geophysics and Astrophysics Monographs. Reidel, Dordrecht.
Ceplecha Z., 1987, Bull. Astron. Inst. Cz., 38, 222.
Ceplecha Z., 1988, Bull. Astron. Inst. Cz., 39, 221.
Denning W.F., 1882, The Observatory, 5, 262.
Hoffmeister C., 1948, Die Meteorströme. Barth, Leipzig.
Jenniskens P., 2004, AJ, 127, 3018.
Jenniskens P., 2006, Meteor Showers and their Parent Comets. Cambridge University Press.
Jenniskens P., Brower J., Martsching P., Lyytinen E., Entwistle D., Cooke W. J., 2008, Central Bureau Electronic Telegrams, 3652, 1.
Jenniskens P., 2013, Central Bureau Electronic Telegrams, 3652, 1.
Koten P., Borovička J., Spurny P., Betlem H., Evans S., 2004, A&A, 428, 683.
Lindblad B.A., 1971a, Smiths. Contr. Astrophys., 12, 1.
Lindblad B.A., 1971b, Smiths. Contr. Astrophys., 12, 14.
Madiedo J.M., Trigo-Rodriguez J.M., 2008, Earth Moon Planets, 102, 133.
Madiedo J.M., Trigo-Rodriguez J.M., Ortiz, J.L., Morales, 2010, Advances in Astronomy, 2010, 1. doi:10.1155/2010/167494
Madiedo, J.M., Trigo-Rodríguez, J.M., Williams, I.P., Ortiz, J.L., Cabrera, J., 2013a, MNRAS, 431, 2464.
Madiedo, J.M., Trigo-Rodríguez, J.M., Lyytinen E., Dergham J., Pujols P., Ortiz, J.L., Cabrera, J., 2013b, MNRAS, 431, 1678.
Madiedo J.M., Trigo-Rodríguez, J.M., Konovalova N., Williams I.P., Castro-Tirado A.J., Ortiz J.L., Cabrera J., 2013c, MNRAS, 433, 571.
Madiedo J.M., Trigo-Rodríguez J.M., Williams I.P., Ortiz J.L., Cabrera J., 2013d, MNRAS, 431, 2464
Madiedo J.M., Ortiz J.L., Morales N., Cabrera-Caño J., 2013, MNRAS, 439, 2364.
Madiedo J.M., 2014, Earth Planets and Space, 66, 70.
Madiedo J.M. et al., 2014, MNRAS, 445, 3309.
Madiedo J.M., 2015, MNRAS, 448, 2135.
Moore C.E., 1945, In: A Multiplet Table of Astrophysical Interest. Princeton University Observatory, Princeton, NJ. Contribution No. 20.
Picone J.M., Hedin A.E., Drob D.P., Alkin A.C., 2002, Journal of Geophysical Research (Space Physics), 107, pp. SIA 15-1, DOI: 10.1029/2002JA009430
Rendtel J., Molau S., 2010, WGN, Journal of the IMO, 38, 161.
Southworth R.B., Hawkins G.S., 1963, Smithson Contr. Astrophys., 7, 261.
Trigo-Rodríguez J.M., 1989, WGN. Journal of IMO, 17, 156.
Trigo-Rodríguez J.M. & Llorca J., 2006, MNRAS, 372, 655.
Trigo-Rodríguez J.M. & Llorca J., 2007, MNRAS, 375, 415.
Trigo-Rodríguez J.M., Madiedo J.M., Williams I.P., 2009, MNRAS, 394, 569.
Williams I.P., 2011, A&G, 52, 2.20.